RSC Advances

ROYAL SOCIETY OF CHEMISTRY

www.rsc.org/advances

Enhanced Thermoelectric Performance in Metal/Semiconductor Nanocomposite of Iron Silicide/Silicon Germanium

Amin Nozariasbmarz,[1,*] Zahra Zamanipour,[2,*] Payam Norouzzadeh,[2] Jerzy S. Krasinski[2] and Daryoosh Vashaee[1,†]

[1]Electrical and Computer Engineering Department, Monteith Research Center, North Carolina State University, Raleigh, NC 27606, USA

[2]School of Electrical and Computer Engineering, Helmerich Advanced Technology Research Center, Oklahoma State University, Tulsa, OK 74106, USA

* A.N. and Z.Z. contributed equally in this work.
† Author to whom correspondence should be addressed. Electronic mail: dvashae@ncsu.edu, Tel: (919) 515-9599

Abstract

Hypothetical efficient thermoelectrics based on nanoparticle in alloy of silicide nanocomposites were predicted by *Mingo et al.* [1]. This investigation presents the experimental realization of n-type silicon germanium alloy with embedded metallic α-phase iron silicide ($FeSi_2$). The dimensionless thermoelectric figure of merit (*ZT*) of the nanocomposite material was higher than the peak *ZT* of the conventional single phase $Si_{0.80}Ge_{0.20}$ over a broad temperature range (650 ˚C ~ 1000 ˚C) while consuming smaller amount of germanium. The addition of 2.5% silver to the nanocomposite, which acted as sintering aid, reduced the sintering temperature and resulted in smaller thermal conductivity. The optimum material composition of $(Si_{0.88}Ge_{0.12})_{0.925}$-$(FeSi_2)_{0.05}$-$Ag_{0.025}$ was found after investigation of a large number of nanocomposite materials. The combination of X-ray diffraction, energy-dispersive X-ray spectroscopy, and transmission electron microscopy analysis confirmed uniform distribution of α-$FeSi_2$ nanoparticles in the microstructure.

Keywords: Metal semiconductor nanocomposite, Silicon germanium, Iron silicide, Nanoparticles, Thermoelectric properties.

Introduction

The prospect of the heavily doped silicon germanium (SiGe) alloys as a high temperature thermoelectric (TE) material up to 1100 ˚C was confirmed in 1960s [2-4]. Since then the synthesis process and properties of SiGe alloy have been extensively studied both theoretically and experimentally in order to further improve its TE properties [5-11]. The efficiency of the TE materials is presented by dimensionless TE figure-of-merit, *ZT*, of the material according to equation (1),

$$ZT = \frac{\sigma S^2}{\kappa} T \quad (1)$$

in which S, σ, T, and κ are the Seebeck coefficient, electrical conductivity, absolute temperature, and the thermal conductivity, respectively. The total thermal conductivity consists of lattice, electronic, and bipolar contributions [5,12].

In 1990s, low dimensional nanostructuring approach was proposed to increase the *ZT* in TE materials via the power factor ($S^2\sigma$) enhancement and the thermal conductivity reduction [13]. The thermal conductivity reduction arises due to the scattering of phonons at interfaces in the nanostructures. Although vast number of experimental reports confirmed the reduction of thermal conductivity through nanostructuring, there has been much less success to demonstrate the improvement of the power factor. Nano bulk structures such as nanostructured $(Bi,Sb)_2Te_3$ [14,15], Si [16,17], and SiGe [18] also showed similar positive trends of the *ZT* improvement although some other materials like Mg_2Si and $MnSi_{1.7}$ did not show remarkable or any improvement by nanostructuring [19,20]. In particular, both p type and n type nano bulk $Si_{0.80}Ge_{0.20}$ showed enhanced *ZT* with values of approximately 0.9 [18] and 1.3 [21] near 1000 ˚C, respectively. It should be noted that *ZT* measurements can have up to 20% tolerance even with today's commercial instruments [22]. In addition, inappropriate sample geometries can affect the data and add to the instrument tolerance. Therefore, reporting *ZT* values from different works may not be an accurate comparison. Moreover, the peak *ZT* is not the only important quantity. When the temperature differential across the thermoelectric leg is large, the value of *ZT* over the whole temperature range can be more important than the peak *ZT*. Therefore, it is important to engineer materials with broad peak *ZT* versus temperature [23].

Numerous composite materials have been also investigated for thermoelectric applications. The optimization of the composite structure was studied in 1991 [24] to enhance the TE power factor. Later in 1999, an effective-medium theory was developed to calculate the power factor of a two component composite material [25]. It was shown theoretically that the power factor of a two component composite material can be increased with respect to that of each individual material, but the maximum *ZT* of the composite cannot be higher than that of the constituting materials. In this model, neither the grain boundary region nor the nano-scale effects were considered in the calculations. Several experimental studies have shown power factor enhancement for materials such as $Si/Si_{0.80}Ge_{0.20}$ [26], InGaAs/ErAs [27,28] SiGe-$CrSi_2$ [29] and BiSbTe [30].

Kim and *Majumdar* [31] proposed the effect of dispersed spherical nanoparticles on the thermal conductivity of a material. *Mingo et al.* [1] theoretically predicted promising nanocomposite alloys with embedded nanoparticles specifically for silicide-SiGe nanocomposite. They confirmed the previous studies that the thermal conductivity can be decreased lower than the alloy limit via nanostructuring of the SiGe alloys to enhance the *ZT*. Furthermore, they discussed that silicide nanoinclusions in SiGe can improve the TE power factor through preferential scattering of the low energy charge carriers.

In the present work, iron disilicide ($FeSi_2$) and silver were chosen as the nanoinclusions in SiGe matrix. $FeSi_2$ has two different phases: (1) β-$FeSi_2$ is a low temperature phase, which has orthorhombic structure and semiconducting properties with thermoelectric characteristics, (2) α-$FeSi_2$ is a high temperature phase, which has tetragonal structure with metallic properties [32,33]. The nanocomposite samples were synthesized by ball milling and sintering procedure. The effect of silver addition, as a sintering aid, was further studied to reduce the sintering temperature and enhance the electrical binding. The microstructure and thermoelectric properties

of the synthesized materials were studied in detail. The results showed that a significant reduction of the thermal conductivity is possible, which would improve the *ZT*. Moreover, the reduced amount of Ge in $Si_{0.88}Ge_{0.12}$ composite structure offered a more cost-effective material with thermal conductivity as low as that of the nanostructured $Si_{0.80}Ge_{0.20}$ alloy [21].

Experimental Methods

$Si_{0.88}Ge_{0.12}$ and $FeSi_2$ powders were prepared separately using high energy ball milling. Stoichiometric ratio of Si (99% purity), and Ge (99%) with 2 atomic % (at.%) P (99.9% purity) were weighted and loaded in a tungsten carbide bowl. We will refer to $Si_{0.88}Ge_{0.12}$ as SiGe in this work from now on. The bowl was sealed inside an argon filled glove box and the load was subsequently milled in a planetary ball mill (Fritsch-P7PL). The $FeSi_2$ powder was separately prepared in a similar way with stoichiometric ratio of Si (99% purity), and Fe (99.99% purity). Several different composite powders were prepared according to the following compositions: SiGe-5%$FeSi_2$, SiG-5%$FeSi_2$-2.5%Ag, and SiGe-5%$FeSi_2$-5%Ag [34]. The percentages are at.% of each material in the composite material. All powders were milled in Fritsch-P7PL planetary ball mill under argon atmosphere at 1000 rpm for 50 hours. The powder was collected and sintered in a graphite die with an internal diameter of 12.7 mm. Numerous samples were consolidated using a customized direct current heating hot press system. The samples were characterized in order to optimize the sintering conditions and attain the largest *ZT*. The main sintering parameters were the sintering temperature, soaking time, and the pressure. The samples were cut into rectangular bars (~ 2 mm × 2 mm × 12 mm) for electrical conductivity and Seebeck coefficient measurement, and circular disks (~12.7 mm in diameter and ~1.5 mm in thickness) for thermal conductivity measurement.

Table 1 shows the sintering parameters, thermal conductivity (at maximum *ZT*) and maximum *ZT* of the composite materials. The data related to the thermal conductivity and *ZT* will be discussed in detail in a subsequent section.

Table 1: Sintering parameters, thermal conductivity and maximum *ZT* of the synthesized nanocomposite materials

ID	Material	Sintering Temperature (˚C)	Soaking time (min)	Pressure (MPa)	Thermal conductivity ($Wm^{-1}K^{-1}$)	*ZT*
1	SiGe-5%$FeSi_2$	1170	0	138	4.0	0.9
2	SiGe-5%$FeSi_2$-2.5%Ag	1050	0	138	4.7	0.9
3	SiGe-5%$FeSi_2$-2.5%Ag	1000	15	138	2.8	1.2
4	SiGe-5%$FeSi_2$-5%Ag	1000	15	138	4.5	1.0

The sintered samples were characterized by X-ray diffraction (XRD) using a Bruker AXS D8-Discover with Cu-K_α radiation apparatus at 2θ angles of 10-60˚. The identification of phases and the crystallite size were determined using the diffraction spectrum. The mean crystallite size of the samples were calculated using commercial software (DiffractPlus EVA 14, Brucker-AXS) which uses a full pattern matching (FPM) of the XRD data based on empirical model for the peak shape and pseudo Vigot functions for fitting the data. The software calculates the crystallite size by the corrected Scherrer's formula for the instrumental broadening [35]:

$$L = \frac{k\lambda}{cos\,\theta\sqrt{U^2 - S^2}} \quad (2)$$

where k is the *Scherrer* constant, a shape factor which is 0.89, λ is the wavelength of Cu-K_α (λ = 1.54 Å) and $\sqrt{U^2 - S^2}$ is integral breath for *Gaussian* profile. U is the FWHM of the undisclosed peaks and S is the instrument broadening in radian.

The microstructure and elemental distribution of the elements in the sintered samples were characterized by a Hitachi S-400 scanning electron microscope (SEM), equipped with an Oxford Instrument energy dispersive spectrometer (EDS), and transmission electron microscope (TEM, JEOL-JEM-2100), respectively. Electrical conductivity and Seebeck coefficient were measured by four probe method using the commercially available Ulvac ZEM-3 instrument in the range of 28-950 ˚C. The sample contact to the electrical leads and the thermocouples for Seebeck coefficient measurement were devised carefully to minimize the measurement errors. Thin carbon films (70 micrometer thick) were mounted at the tip of the thermocouple probes to prevent any reaction between the sample and the thermocouples and falsification of the data. The carbon film did not affect the temperature measurement, which was verified with measuring a known reference sample (constantan) from room temperature to 1000 ˚C. The thermal conductivity (κ) of the samples was calculated according to:

$$\kappa = \alpha \rho C_p \quad (3)$$

where α is the thermal diffusivity measured using the laser flash instrument (Netzsch's LFA 457 Micro Flash), ρ is the mass density of the sample measured using the *Archimede*s' principle, and C_p is the specific heat. A Pyroceram disk was used as the reference sample in the laser flash apparatus to determine the specific heat of the samples.

Results and Discussions

The XRD data of samples 1, 3 and 4 are shown in Figure 1. The peaks for SiGe, α-$FeSi_2$ and Ag were identified in the spectra, which are marked with the symbols. The XRD data confirms that the $FeSi_2$ has formed in its tetragonal structure (α-phase and metallic) and not orthorhombic structure (β-phase and semiconductor). A more precise characterization method such as EDS and SAED pattern was performed to identify the silver and α-$FeSi_2$ phases in the matrix. The XRD data shows that SiGe is completely alloyed and there is no elemental impurity in the material or it is less than the detectable limit by the XRD machine. The mean crystallite size of the SiGe in sample 3 was estimated to be in the range of 30 nm.

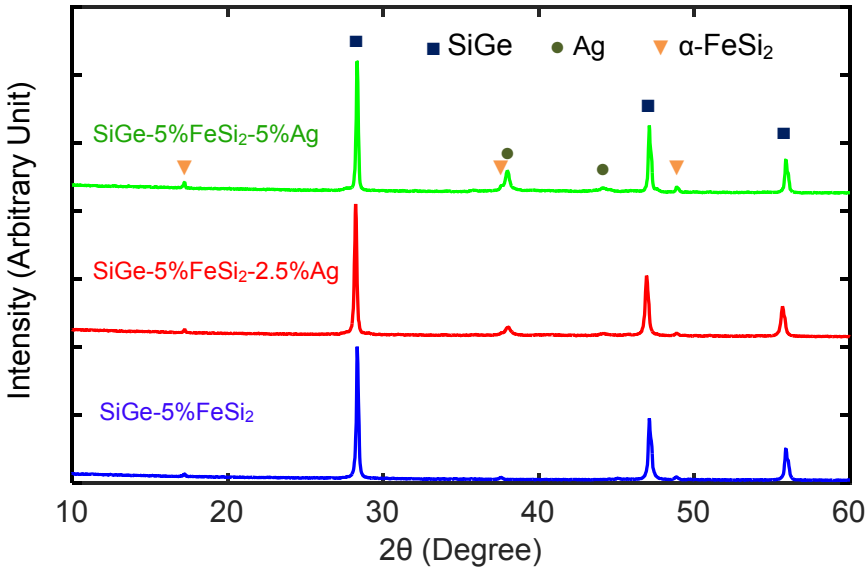

Figure 1: XRD patterns of the composite sample 1 (SiGe-5%$FeSi_2$), sample 3 (SiGe-5%$FeSi_2$-2.5%Ag) and sample 4 (SiGe-5%$FeSi_2$-5%Ag).

Figure 2 shows the SEM micrograph and the EDS map of a cleaved surface of the composite sample 3. The morphology and the homogeneity of the sample is observable. SEM image depicts bright nanoparticles which are uniformly distributed in a matrix. The EDS maps separately show

the presence of each element. Si, Ge and P elements show a fairly uniform distribution in the EDS maps and with no significant segregation in the microstructure. The 2 at.% phosphorous was added to SiGe as an n-type dopant to tune the electrical conductivity and the Seebeck coefficient and to achieve the maximum thermoelectric power factor. This often requires high amount of P close to its solubility limit in SiGe [8]. The solubility of P in $Si_{1-x}Ge_x$ is a function of temperature and x. The exact solubility of P in $Si_{0.88}Ge_{0.12}$ is not known; however, its value is expected to be close to and smaller than the solubility limit in Si [36]. P solubility in Si increases from ~1.2 at.% at 920 ˚C to 1.8 at.% at 1310 ˚C [37]. P solubility in polycrystalline $Si_{0.8}Ge_{0.2}$ is reported to be ~0.2 at.% at room temperature [38]. We have intentionally added excessive P to the initial powder mixture to assure reaching the solubility limit of P in $Si_{0.88}Ge_{0.12}$ and to compensate for any material loss that may happen during the milling and material synthesis process. Therefore, it is expected that P precipitations form at room temperature, which can explain the observed particles in the EDS map of the P atoms.

The EDS map of Fe, however, shows a uniform distribution of larger size Fe-rich domains, which indicates that the bright spots in the SEM image are associated with $FeSi_2$ nanoinclusions. Due to the nature of powder processing by mechanical alloying, $FeSi_2$ particles are uniformly dispersed in the SiGe powder. At sintering temperature below the melting point of both SiGe and $FeSi_2$ the uniform distribution of these particles is maintained in the matrix. However, if the sample melts during consolidation, $FeSi_2$ particles may have the chance to diffuse into each other and make larger particles in the matrix. Therefore, one would prefer to sinter the sample below the melting point of the constituent components. It should be noted that too small sintering temperature can cause low density or poor electrical bonding among the grains resulting in small carrier mobility and thermoelectric power factor. Therefore, there exists an optimum sintering

temperature to reach high power factor while maintaining the nanocomposite morphology of the sample and reducing the thermal conductivity. For comparison, the EDS map of the silver does not show significant agglomeration as silver, with melting point of ~960 ˚C, melts during sintering of these samples. However, since the sintering temperature is below melting point of $FeSi_2$, i.e. ~1220 ˚C, the agglomerated $FeSi_2$ particles still exist in the consolidated samples.

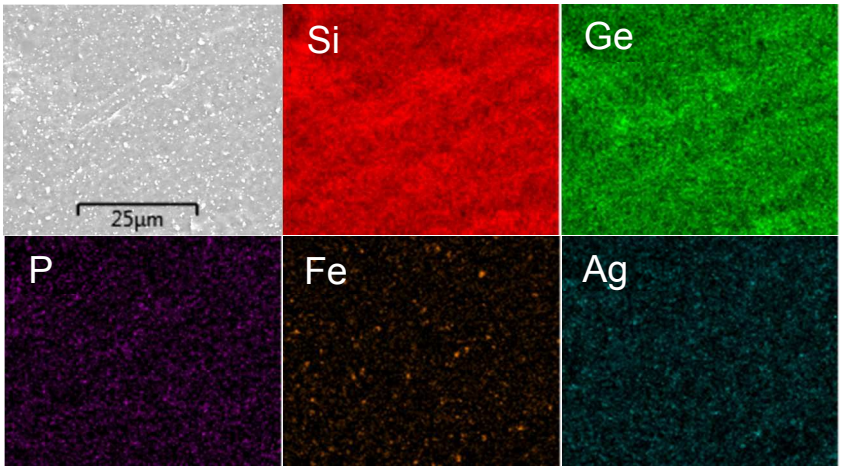

Figure 2: SEM image and EDS map of sample 3. Uniform dispersion of Fe-rich domains indicate the presence of $FeSi_2$ nanoinclusions in the microstructure.

Figure 3 shows the bright field TEM image and the selected area electron diffraction (SAED) pattern of sample 3. It confirms the composite structure in which α-$FeSi_2$ is embedded in a large SiGe grain. A number of dispersed nanoparticles with dimensions of less than 10 nm can be clearly seen in the microstructure. These small particles with random orientations can efficiently scatter phonons and reduce the thermal conductivity of the samples. Due to the large variation between the mean free path (MFP) of electrons and phonons (cartoon shown in Figure 3), the reduction of the phonon thermal conductivity is more than that of the electrical conductivity [21]. The nanoparticles consist of α-$FeSi_2$ phases which are distributed in SiGe background. The

analysis of SAED pattern confirms the existence of SiGe, α-$FeSi_2$ and Ag phases in the microstructure, which is consistent with the XRD pattern and EDS map.

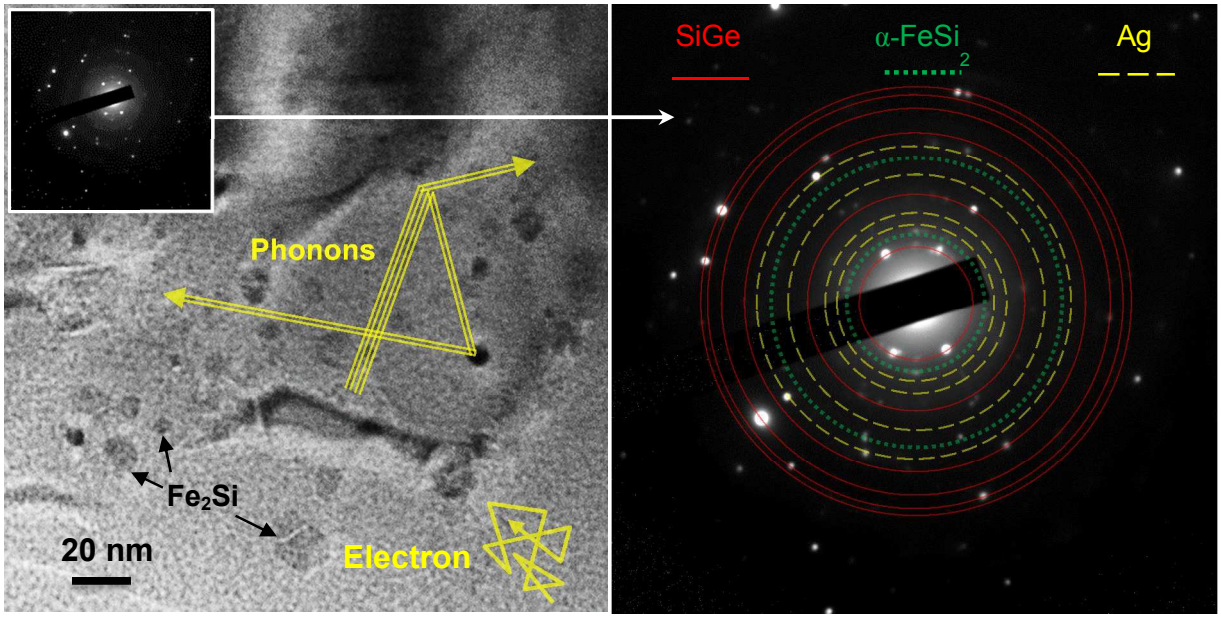

Figure 3: TEM image and SAED pattern of sample 3. α-$FeSi_2$ nanoparticles are embedded in SiGe host as marked with arrows. A cartoon of the electron and phonon mean free paths is also shown by lines and arrows. SAED pattern shows the existence of SiGe, α-$FeSi_2$ and Ag phases.

It is known that nanoparticles can decrease the thermal conductivity below the alloy limit. In brief, nanoparticles can act as scattering centers with cross section, σ_s. The scattering cross section of a spherical nanoparticle at low frequencies may be estimated according to [39]:

$$\sigma_s = \frac{q^4(\delta M)^2}{4\pi\rho^2} \quad (4)$$

where q is the wave vector, δM is the total extra mass of the nanoparticle and ρ is the density of the medium. Equation (4) indicates that the cluster of N atoms of the second phase embedded in the matrix can scatter low frequency phonons by a factor of N^2, which is N time more than N single atoms. This scenario is different at high frequencies where σ varies with $N^{2/3}$, which is $N^{1/3}$

times smaller than scattering from N single atoms [1]. Therefore, clustering enhances scattering of low frequency phonons more than high frequency phonons. According to the *Mathiessen*'s rule (Equation (5)), the cooperative scattering by the individual atoms in the alloy (Λ_a) and the clusters of the second phase (Λ_c) would result in a smaller MFP than each of them individually resulting in further decrease of the thermal conductivity [1].

$$\frac{1}{\Lambda} = \frac{1}{\Lambda_a} + \frac{1}{\Lambda_c} \tag{5}$$

The nanoparticles also scatter electrons. However, the scattering rate from nanoparticles is expected to be smaller than the sum of other scatterings, mainly the scattering by ionized impurities and acoustic phonons [9]. Therefore, the electrical conductivity is not affected as much as the thermal conductivity.

Figure 4 shows the (a) electrical conductivity, (b) Seebeck coefficient, (c) Power factor times temperature (PFT), and (d) thermal conductivity of the synthesized composite materials as a function of temperature in the range of 27-1000 ˚C. The data of a crystalline $Si_{0.80}Ge_{0.20}$ used in radioisotope thermoelectric generators (RTG) is also shown with solid line for comparison [18].

Sample 4 with 5% silver, which is the highest concentration of Ag in this study, has the highest electrical conductivity in the whole temperature range. The large electrical conductivity of sample 4 can be associated to high carrier concentration and/or high carrier mobility. Since the Seebeck coefficient is a strong function of the carrier concentration (n) [40], the comparison of the Seebeck coefficients, as shown in Figure 4-b, indicates the strengths of the carrier concentrations in the samples. The smallest absolute Seebeck coefficient of sample 4 compared to the other samples indicates that sample 4 has the highest carrier concentration (n). The electrical conductivity (σ) depends on both the carrier concentration (n) and the carrier mobility

(μ), i.e. $\sigma=en\mu$. Therefore, the large electrical conductivity of sample 4 is associated to its high carrier concentration. Moreover, comparing sample 4 (with 5% Ag) with sample 2 (with 2.5% Ag), one would notice a large difference in the electrical conductivity while the Seebeck coefficient is not significantly different. This difference would further indicate the higher carrier mobility of sample 4. The higher carrier mobility may be associated with higher concentration of silver in this sample. Silver is expected to improve the bonding of the grains during sintering due to its lower melting point (~960 ˚C) than those of SiGe (~1337 ˚C) and $FeSi_2$ (~1220 ˚C). During sintering, Ag melt can also fill the pores among the grains, which would further improve the electrical bonding; hence, the carrier mobility.

The reducing slope of the electrical conductivity with temperature in all samples is due to the decrease of the carrier mobility, which is originated from the increase of the acoustic phonon scattering with temperature. At temperatures above 800 ˚C, a small increase in the electrical conductivity of the samples was observed. At the same temperature, the absolute Seebeck coefficient decreased and the thermal conductivity increased. This change can be associated to both dopant activation and increase of the intrinsic carriers at high temperature [9,41]. The samples are doped with phosphorous to their solid solubility limit which is a function of temperature. Therefore, the electron concentration increases once more dopants are activated and improve the carrier conductivity. A similar trend is observed for the RTG sample; however, it starts at slightly lower temperature close to ~700 ˚C. For example, sample 1 and the RTG sample show similar electrical conductivity and the Seebeck coefficient from room temperature up to ~600 ˚C. Above this temperature both properties increase for the RTG sample while their increase for sample 1 is pushed to above 900 ˚C (the slope change is observed at ~800 ˚C). Such a different trend is associated with the larger bandgap of the samples studied in this work. The

RTG sample, i.e. $Si_{0.80}Ge_{0.20}$, has smaller bandgap than $Si_{0.88}Ge_{0.12}$, which results in larger thermal excitation of the minority carriers. The effect, which is often known as bipolar transport, increases the electrical conductivity, reduces the absolute Seebeck coefficient, increases the thermal conductivity, and overall reduces the *ZT*.

Sample 2 has the highest Seebeck coefficient and lowest electrical conductivity over the entire temperature range, which indicates its lower carrier concentration compared to the other samples.

From room temperature to 400 ˚C, the power factor is approximately similar for all the composite structures (Figure 4-c) and it starts to differentiate at higher temperatures. The highest power factor time temperature (PFT) of 4.5 $Wm^{-1}K^{-1}$ belongs to sample 4, which has also the highest electrical conductivity. The other samples have approximately similar PFT.

A wide variation of the thermal conductivity is observed for different nanocomposite samples. In general, the thermal conductivity decreases with temperature due to the increase of phonon-phonon scattering. The thermal conductivity increases above 800 ˚C due to ambipolar thermal diffusion. Samples 1 and 2 were hot pressed with zero soaking time, which must have resulted in smaller grain growth and higher phonon-grain boundary scattering in the sample. Sample 2 and sample 3 have identical composition, but sample 3 was hot pressed at smaller temperature (1000 ˚C) and with higher soaking time (15 min). The smaller sintering temperature of sample 3, even with longer soaking time, resulted in lowest thermal conductivity among all samples. The thermal conductivity of sample 3 is approximately equal to that of amorphous silicon at room temperature and twice of that at high temperature [42]. Samples 3 and 4 were sintered under identical conditions; however, sample 4 had higher thermal conductivity, which can be associated with its higher concentration of silver. Therefore, it can be concluded that the optimum amount of silver is less than 5%.

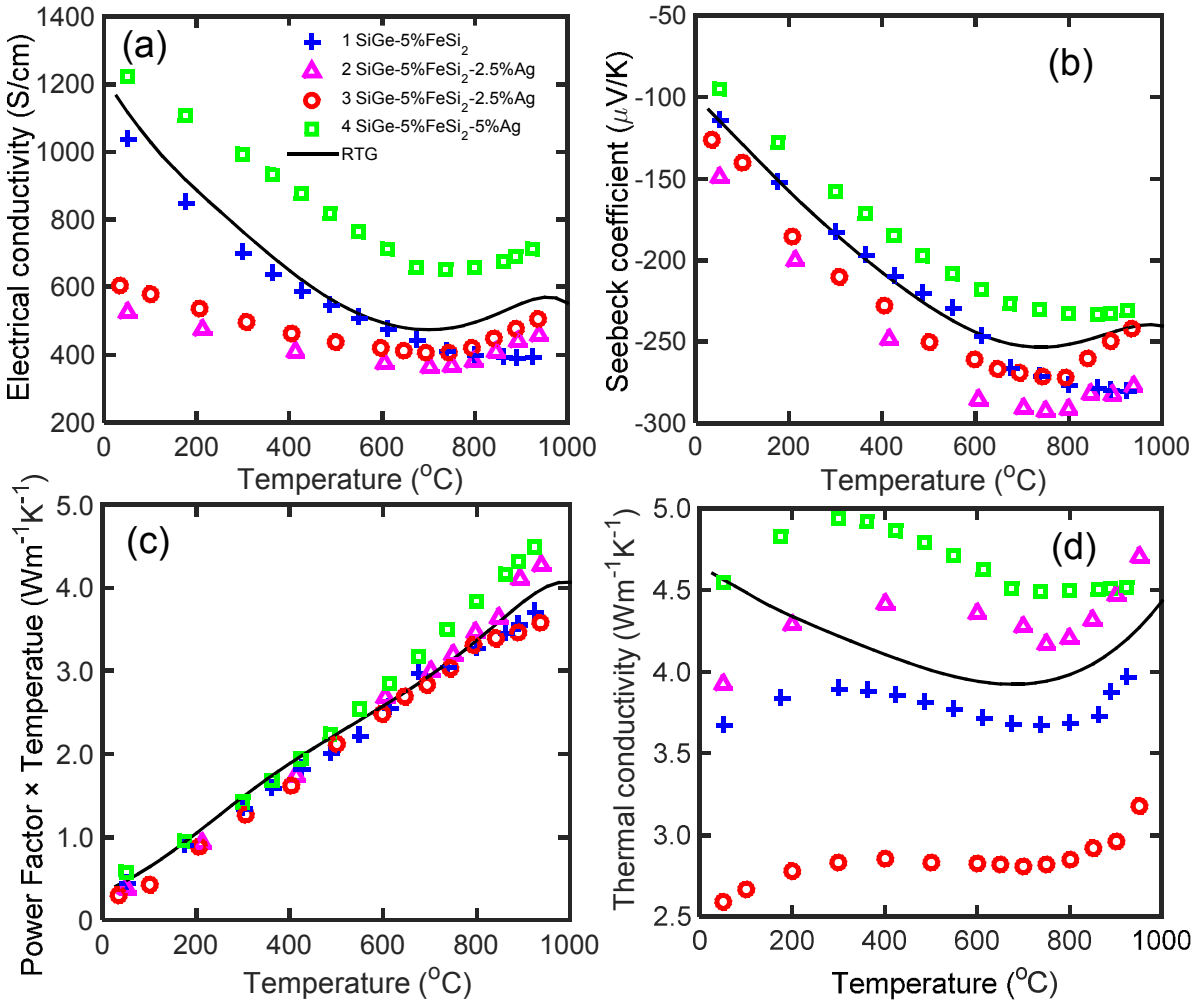

Figure 4: (a) Electrical conductivity, (b) Seebeck coefficient, (c) Power factor times temperature, and (d) Thermal conductivity of the synthesized nanocomposite samples versus temperature (symbols). The solid line shows the data of the RTG sample.

The comparison of *ZT* versus temperature for all the samples is shown in Figure 5. Sample 1, 2 and 4 have nearly similar *ZT* over the entire temperature range, which are also similar to that of the RTG sample. The highest *ZT* belongs to sample 3 (SiGe-5%$FeSi_2$-2.5%Ag), which is approximately 1.2 over the temperature range of 800-950 ˚C. It is also interesting to note that the *ZT* remains higher than the conventional single phase $Si_{0.80}Ge_{0.20}$ used in RTGs over a broad

range of temperature (650 ˚C ~ 1000 ˚C) while using smaller amount of germanium. The main reason for the *ZT* enhancement in this sample is associated to the reduction of the thermal conductivity while maintaining the power factor as the other samples.

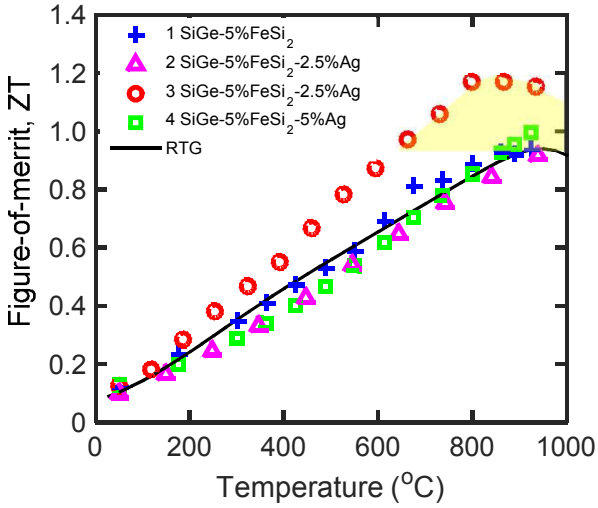

Figure 5: Temperature dependence of the dimensionless figure of merit, *ZT*, for the synthesized nanocomposite materials (symbols) compared to that of the RTG sample (solid line).

Conclusions

The metal-semiconductor nanocomposite of n-type thermoelectric SiGe-$FeSi_2$ was successfully developed and characterized versus electrical, thermal, and microstructural properties. As compared with the theoretical prediction of the optimum silicide nanoparticle size in SiGe matrix, i.e. 3-30 nm [1], $FeSi_2$ nanoinclusions were in the range of 5~20 nm. The optimum sample showed up to 25% higher *ZT* than the peak *ZT* of the conventional $Si_{0.80}Ge_{0.20}$ alloy over the entire range of ~650 ˚C to 1000 ˚C. It also utilized smaller amount of germanium which reduces the material cost. In order to optimize the sintering parameters and the thermoelectric properties, a large number of nanocomposites were synthesized, measured and analyzed. The

sample with 2.5 at.% silver and 5 at.% α-$FeSi_2$ showed the optimum properties. The addition of silver as sintering aid allowed reducing the sintering temperature from 1170 ˚C to 1000 ˚C which resulted in smaller thermal conductivity while maintaining approximately similar thermoelectric power factor, which is the main reason for the observed enhancement of the *ZT*.

Acknowledgment

This study is partially based upon work supported by Air Force Office of Scientific Research (AFOSR) under contract number FA9550-12-1-0225 and the National Science Foundation (NSF) under grant numbers EEC-1160483, ECCS-1351533 and CMMI-1363485. JSK acknowledges the funding support from Oklahoma Center for the Advancement of Science & Technology (OCAST) Oklahoma Applied Research Support (OARS) program under contract number AR14-052.

References

[1] N. Mingo, D. Hauser, N. P. Kobayashi, M. Plissonnier and A. Shakouri, "Nanoparticle-in-Alloy" Approach to Efficient Thermoelectrics: Silicides in SiGe, Nano Lett., **2009**, 9(2), 711–715.

[2] B. Abeles, D. S. Beers, G. D. Cody and J. P. Dismukes, Thermal Conductivity of Ge-Si Alloys at High Temperatures, Phys. Rev., **1962**, 125, 44-46.

[3] J. P. Dismukes, L. Ekstrom, E. F. Steigmeier, I. Kudman and D. J. Beers, Thermal and electrical properties of heavily doped Ge–Si alloys up to 1300 K, J. Appl. Phys., **1964**, 35, 2899-2907.

[4] D. M. Rowe, Thermoelectrics Handbook: Macro to Nano, CRC Press, **2005**.

[5] J. P. Dismukes and L. Ekstrom, Homogeneous solidification of Ge-Si alloys, Trans. Met. Soc. AIME, **1965**, 233, 672-80.

[6] D. M. Rowe and R. W. Bunce, The thermoelectric properties of heavily doped hot-pressed germanium-silicon alloys, J. Phys. D: Appl. Phys., **1969**, 2, 1497-1502.

[7] C.B. Vining, A model for the high-temperature transport properties of heavily doped n-type silicon-germanium alloys, J. Appl. Phys., **1991**, 69, 331-341.

[8] A. Minnich, H. Lee, X. W. Wang, G. Joshi, M. S. Dresselhaus, Z. F. Ren, G. Chen and D. Vashaee, Modeling study of thermoelectric SiGe nanocomposites, Phys. Rev. B, **2009**, 80, 155327-1-14.

[9] Z. Zamanipour, X. Shi, A. M. Dehkordi, J. S. Krasinski and D. Vashaee, The effect of synthesis parameters on transport properties of nanostructured bulk thermoelectric p-type silicon germanium alloy, Phys. Status Solidi A., **2012**, 209(10), 2049–2058.

[10] A. Nozariasbmarz, A. Tahmasbi Rad, Z. Zamanipour, J. S. Krasinski, L. Tayebi and D. Vashaee, Enhancement of thermoelectric power factor of silicon germanium films grown by electrophoresis deposition, Scripta Mater., **2013**, 69(7), 549-552.

[11] M. Abudakka, A. Nozariasbmarz, L. Tayebi, J. S. Krasisnki and D. Vashaee, Development of inexpensive SiGe–$FeSi_2$ thermoelectric nanocomposites, Energy Harvesting and Systems, **2015**, 2(1), 47-53.

[12] C.B. Vining, Handbook of Thermoelectrics, New York: CRC, **1995**.

[13] L. D. Hicks and M. S. Dresselhaus, Effect of quantum-well structures on the thermoelectric figure of merit, Phys. Rev., **1993**, B47, 12727-12731.

[14] B. Poudel, Q. Hao, Y. Ma, Y. Lan, A. Minnich, B. Yu, X. Yan, D. Wang, A. Muto, D. Vashaee, X. Chen, J. Liu, M. S. Dresselhaus, G. Chen and Z. Ren, High-thermoelectric performance of nanostructured bismuth antimony telluride bulk alloys, Science, **2008**, 320, 634-638.

[15] T. Zhang, J. Jiang, Y. Xiao, Y. Zhai, S. Yang and G. Xu, In Situ Precipitation of Te Nanoparticles in p‐Type BiSbTe and the Effect on Thermoelectric Performance, Appl. Mater. Interfaces, **2013**, 5, 3071−3074.

[16] A. Miura, S. Zhou, T. Nozaki, and J. Shiomi, Crystalline−Amorphous Silicon Nanocomposites with Reduced Thermal Conductivity for Bulk Thermoelectrics, Appl. Mater. Interfaces, **2015**, 7, 13484−13489.

[17] S. K. Bux, R. G. Blair, P. K. Gogna, H. Lee, G. Chen, M. S. Dresselhaus, R. B. Kaner and J. P. Fleurial, Nanostructured Bulk Silicon as an Effective Thermoelectric Material, Adv. Funct. Mater., **2009**, 19, 2445–2452.

[18] G. Joshi, H. Lee, Y. Lan, X. Wang, G. Zhu, D. Wang, R. W. Gould, D. C. Cuff, M. Y. Tang, M. S. Dresselhaus, G. Chen and Z. Ren, Enhanced thermoelectric figure-of-merit in nanostructured p-type silicon germanium bulk alloys, Nano lett. **2008**, 8(12), 4670–4674.

[19] N. Satyala and D. Vashaee, The effect of crystallite size on thermoelectric properties of bulk nanostructured magnesium silicide (Mg_2Si) compounds, Appl. Phys. Lett., **2012**, 100, 073107-1-4.

[20] P. Norouzzadeh, Z. Zamanipour, J. S. Krasinski and D. Vashaee, The effect of nanostructuring on thermoelectric transport properties of p-type higher manganese silicide $MnSi_{1.73}$, J. Appl. Phys., **2012**, 112(12), 124308-1-7.

[21] X. W. Wang, H. Lee, Y. C. Lan, G. H. Zhu, G. Joshi, D. Z. Wang, J. Yang, A. J. Muto, M. Y. Tang, J. Klatsky, S. Song, M. S. Dresselhaus, G. Chen and Z.F. Ren, Enhanced thermoelectric figure of merit in nanostructured n-type silicon germanium bulk alloy, Appl. Phys. Lett., **2008**, 93, 193121-1-3.

[22] K. A. Borup, J. de Boor, H. Wang, F. Drymiotis, F. Gascoin, X. Shi, L. Chen, M. I. Fedorov, E. Muller, B. B. Iversena and G. J. Snyder, Measuring thermoelectric transport properties of materials, Energy Environ. Sci., **2015**, 8, 423–435.

[23] G. J. Snyder and T. S. Ursell, Thermoelectric Efficiency and Compatibility, Phys. Rev. Lett., **2003**, 91, 148301-1-4.

[24] D. J. Bergman and O. Levy, Thermoelectric properties of a composite medium J. Appl. Phys., **1991**, 70, 6821-6833.

[25] D. J. Bergman and L. J. Fel, Enhancement of thermoelectric power factor in composite thermoelectrics, J. Appl. Phys., **1999**, 85, 8205-8216.

[26] M. Zebarjadi, G. Joshi, G. Zhu, B. Yu, A. Minnich, Y. Lan, X. Wang, M. S. Dresselhaus, Z. Ren and G. Chen, Power factor enhancement by modulation doping in bulk nanocomposites, Nano Lett., **2011**, 11(6), 2225–2230.

[27] J. M. O. Zide, D. Vashaee, G. Zeng, J. E. Bowers, A. Shakouri and A. C. Gossard, Demonstration of electron filtering to increase the Seebeck coefficient in $In_{0.53}Ga_{0.47}As$/ $In_{0.53}Ga_{0.28}Al_{0.19}As$ superlattices, Phys. Rev. B, **2006**, 74, 205335-1-5.

[28] J. H. Bahk, Z. Bian, M. Zebarjadi, P. Santhanam, R. Ram and A. Shakouri, Thermoelectric power factor enhancement by ionized nanoparticle scattering, Appl. Phys. Lett., **2011**, 99, 072118-1-3.

[29] Z. Zamanipour and D Vashaee, Comparison of thermoelectric properties of p-type nanostructured bulk $Si_{0.8}Ge_{0.2}$ alloy with $Si_{0.8}Ge_{0.2}$ composites embedded with $CrSi_2$ nano-inclusions, J. Appl. Phys., **2012**, 112(9), 093714-1-9.

[30] A. M. Dehkordi and D. Vashaee, Enhancement in thermoelectric power factor of polycrystalline $Bi_{0.5}Sb_{1.5}Te_3$ by crystallite alignment, Phys. Status Solidi A, **2012**, 209(11), 2131-2134.

[31] W. Kim and A. Majumdar, Phonon scattering cross section of polydispersed spherical nanoparticles, J. Appl. Phys., **2006**, 99, 084306-1-7.

[32] M. Mohebali, Y. Liu, L. Tayebi, J. S. Krasinski and D. Vashaee, Thermoelectric figure of merit of bulk $FeSi_2$–$Si_{0.8}Ge_{0.2}$ nanocomposite and a comparison with β-$FeSi_2$, Renew. Energ., **2015**, 74, 940–947.

[33] O. Kubaschewski, "Iron-Binary Phase Diagrams", Berlin: Springer, **1982**.

[34] A. Nozariasbmarz, M. AbuDakka, L. Tayebi and D. Vashaee, Fabrication and Thermoelectric Properties of Bulk $Si_{0.8}Ge_{0.2}$-$FeSi_2$ Nanocomposite, B. Am. Phys. Soc., Denver, Colorado, **2014**.

[35] DIFFRACplus Basic Evaluation Package, EVA 14 user manual, Bruker AXS GmbH, Karlsruhe, Germany, Order no. DOC-M85-EXX002 V14, **2008**.

[36] J. S. Christensen, Dopant diffusion in Si and SiGe, PhD Dissertation, KTH Microelectronics and Information Technology, Stokholm, **2004**.

[37] R. W. Olesinski, N. Kanani and G. J. Abbaschian, The P-Si (Phosphorus-Silicon) System, Bull. Alloy Phase Diagr., **1985**, 6 (2), 130.

[38] D. M. Rowe and N. Savvides, The reversal of precipitation in heavily doped silicon-germanium alloys, J. Phys. D: Appl. Phys., **1979**, 12, 1613-1619.

[39] J. M. Ziman, Electrons and Phonons; Oxford University Press: New York, **2001**.

[40] O. Yamashita and N. Sadatomi, Dependence of Seebeck Coefficient on Carrier Concentration in Heavily B- and P-Doped $Si_{1-x}Ge_x$ ($x \leq 0.05$) System, Jpn. J. Appl. Phys., **1999**, 38, 6394-6400.

[41] Z. Zamanipour, J. S. Krasinski and D. Vashaee, Comparison of boron precipitation in p-type bulk nanostructured and polycrystalline silicon germanium alloy, J. Appl. Phys., **2013**, 113(14), 143715-1-5.

[42] P. Norouzzadeh, A. Nozariasbmarz, J. S. Krasinski and D. Vashaee, Thermal conductivity of nanostructured Si_xGe_{1-x} in amorphous limit by molecular dynamics simulation, J. Appl. Phys., **2015**, 117, 214303-1-6.

Graphical Abstract: